Contents lists available at ScienceDirect

Nuclear Inst. and Methods in Physics Research, B

Full Length Article

Effective combinations of features in predicting the range of incident ions using machine learning

Hideaki Minagawa [a,*], Tomoya Tezuka [b], Hidetsugu Tsuchida [b,c]

[a] *Ion Technology Center Co., Ltd., Tsudayamate, Hirakata, Osaka 572-0128, Japan*
[b] *Department of Nuclear Engineering, Kyoto University, Nishikyo-ku, Kyoto 615-8530, Japan*
[c] *Quantum Science and Engineering Center, Kyoto University, Gokasho, Uji, Kyoto 611-0011, Japan*

ARTICLE INFO

ABSTRACT

Machine learning techniques were used to predict the range of ions in material, even when stopping power data is unknown. Simple features such as atomic and mass numbers were used in learning process. Two different machine learning models, Decision Tree (DT) and Kernel Ridge Regression (KRR), were used to assess each feature's importance and the effect of combining them. The results showed that the chosen features were sufficient for accurate prediction. Furthermore, it was found that the combination and features are essential for accurate results. Analysis by KRR established a relationship between the range of the implanted ions and the energy of the incident ions, showing that the range is approximately proportional to the energy in the dataset used in this work.

1. Introduction

The ion implantation process is crucial in producing semiconductor devices [1–3]. To regulate the electrical properties of these devices, it is necessary to have a uniform depth distribution of dopant, also known as a box profile. Achieving this requires implanting ions at varying energies. Accurately predicting the implanted ion distribution for each energy is vital to minimize the expenses of prototype device production during research and development.

In the 1980s, researchers aimed to obtain a universal function for the projected range of combinations of incident ions and targets [4–6]. This research introduced reduced energies or ranges, and a universal relationship was obtained through dimensionless calculations. However, the function was only available for energies between 10^{-5} and 1 (dimensionless). The TRIM (Transport of Ions in Matter) Monte Carlo simulation code [7] has made it possible to predict the range of implanted ions using the stopping power data. This simulation calculates the depth distribution of implanted ions in a single target with abundant stopping power data. This simulation accounts for collision processes such as ion scattering and energy loss to provide accurate results.

However, predicting the range of implanted ions for compounds without extensive stopping power data is challenging [8,9]. In calculating the stopping power of a compound, the TRIM code uses a core-and-bond (CAB) model, which determines stopping power and considers differences in bond types within a compound (single and double bonds, etc.). Although it can be used to determine the stopping power of organic molecules, it cannot be applied to determining the stopping power of compound semiconductors, which is the issue in this research.

Formulation of the projected range has also been studied for some compound semiconductors. Janson *et al.* reported that an energy-dependent function could predict the projected range for the SiC target [10]. However, there are still issues related to its generalizability to other targets, such as the generalization of fitting parameters and the usefulness of the function for other materials.

Machine learning has recently been applied in various fields. In particular, it has been used to study stopping power by employing several machine-learning techniques. This allows for predicting stopping power for any ion-target combination over a wide energy range, even when experimental data is unavailable [11,12]. Accurate stopping powers derived from such machine learning techniques can be used in simulations, such as TRIM, to make precise ion range calculations for any given conditions. However, further research is still needed on machine learning to predict the range directly from the information of incident ions and targets without using the stopping power.

In this work, we utilized machine learning to create a model that can predict the range of implanted ions even when the stopping power is

unknown. We used simple parameters such as atomic or mass numbers as the machine learning features. The focus was on the projected range of implanted ions rather than the total range. This is because the projected range is the vertical depth of implanted ions, which can be directly determined from experiments, while the total range is the actual path length of implanted ions. The data for the implanted ion range used for machine learning was experimental data such as secondary ion mass spectrometry (SIMS) profiles. We identified compelling features for accurate prediction of the projected range. This method enables us to quickly expand to other implantation conditions, such as channeling implantation, by including the implantation angle as one of the features of machine learning. Moreover, by changing the objective value from the projected range to the straggling of the implanted ion distribution, we can obtain the overall distribution of ions, like TRIM, even under conditions where the stopping power data is unavailable.

2. Method

2.1. Dataset

Our research collected data on the projected range of implanted ions from various references [5,8,10,17–80]. Table 1 shows a summary of the dataset used in this work. We used 9 single elements and 10 compounds as targets. N_{Ion} denotes the number of ions for each target. N_{Data} shows the total amount of data for each target. The table shows that the data were biased toward specific targets such as C, SiC, or SiO_2. This is because we searched papers that reported the projectile range and the incident energy covering wide range of ion species and energy ranges with a high priority. The distribution of several data could have been different if the focus had been on a specific target, for example, Si, which should have been more widely reported because of its widespread use in semiconductor manufacturing. Detailed information on the references is given in the Appendix. Some studies have found a relationship between reduced ranges and reduced energies (dimensionless), which were then translated into distance expressed in micrometers (μm) and ion energies expressed in kilo electronvolts (keV).

We considered seven features related to the implanted ion and the target materials. These features are ion implantation energy E_0, ion atomic number Z_1, ion mass number M_1, target atomic number Z_2, target mass number M_2, target density ρ [g/cm^3], and the mean excitation energy I [eV] [13]. The feature I added was to consider the electronic properties of the target, which cannot be expressed solely by atomic number and is adoptable for compound targets. For compound targets,

Table 1

Summary of dataset used in this work. N_{Ion} and N_{Data} denote the number of ions and total amount of the data for each target.

TARGET	N_{Ion}	N_{Data}
C	40	225
Si	10	43
V	4	11
Ge	3	23
Zr	2	7
Ag	5	13
W	2	14
Au	13	15
U	1	1
Al_2O_3	12	41
SiO_2	18	125
GaAs	12	58
InSb	1	10
MgO	1	1
LiF	2	16
Si_3N_4	5	5
GaP	2	2
SiC	10	116
GaN	12	13
Total: 19 targets	68	739

we calculated the average value for each feature based on the number density of constituting atoms. For instance, the average atomic number for Al_2O_3 is calculated as the weighted average of the atomic numbers of Al and O: $Z_{Al_2O_3} = 0.4Z_{Al} + 0.6Z_O = 10$, where $Z_{Al} = 13$ and $Z_O = 8$. Regarding the mean excitation energy, we have used Bragg's rule on Bethe's stopping power to obtain the average value from the following relationship: $Z_{Al_2O_3}\ln I_{Al_2O_3} = 0.4Z_{Al}\ln I_{Al} + 0.6Z_O\ln I_O$, assuming an above average atomic number.

Fig. 1 provides an overview of the data processing methods used in this work. We transformed the projected range and ion energy to $R = \log R_p$ and $E = \log E_0$ to achieve high prediction accuracy across a wide range of logarithmic values. Additionally, we standardized each feature by rescaling it with a zero mean and unit variance before every learning. We used the k-fold cross-validation method to choose the training and test data for machine learning. The standardized data was randomly divided into ten groups, and one of these groups was used as test data, while the remaining nine was used as training data. This learning process was repeated ten times with each data group as test data to obtain universal learning results. We performed random data splitting and the k-fold cross-validation ten times to reduce the effects of data splitting. We used these training and test data sets in decision tree or kernel ridge regression to obtain Figs. 2-5. Below is a description of each machine-learning model and script used on the right-hand side of the figure.

2.2. Decision tree (DT) model

The DT model is famous for regression and classification tasks due to its simplicity and interpretability. A DT consists of a set of conditions that are arranged hierarchically. When an input is given, the conditions are applied successively from the root to a terminal node of the tree. This hierarchical structure provides simplicity and interpretability to the DT. To build a DT, essential features are first selected. The process involves splitting the objective values (root) into binary pieces for the regression tree, where the child nodes can reduce error more than the parent node for example, the energy E can either be larger than a certain threshold E_{th} or not. In the regression tree, the predicted result is the average value of the node. The DT then searches through all candidate splits to find the optimal split that minimizes the error of the resulting tree.

This study used the Classification and Regression Tree (CART) models [14] in the Scikit-learn package [15]. We used the mean squared error to obtain residuals for the induction of trees. We chose the default parameters for the DT provided by the Scikit-learn package only to assess the importance of the features.

2.3. Kernel ridge regression (KRR) model

The KRR model is an algorithm for similarity-based learning [16]. We utilized KRR with a Gaussian kernel for machine learning to evaluate various feature combinations. We used the Scikit-learn package [15] for KRR. In this model, to predict an objective value of a new system, we estimate it by summing up weighted kernel functions (Gaussians) over the entire training sets (amount of the training sets is N_{train}). The prediction of a KRR objective Y can be represented mathematically as follows:

$$Y_j^{\text{pred}} = \sum_i^{N_{\text{train}}} w_i \exp\left(-\frac{\left|\mathbf{d}_i - \mathbf{d}_j\right|^2}{2\sigma^2}\right) \tag{1}$$

In the above equation, i and j are the systems in the training set and the new system (prediction), σ is the width of the Gaussian kernel, and $\left|\mathbf{d}_i - \mathbf{d}_j\right|^2$ is the squared Euclidean distance between the feature vectors $\mathbf{d}_i$ and $\mathbf{d}_j$. The training dataset's small Euclidean distance between the feature vectors $\mathbf{d}_i$ and $\mathbf{d}_j$ affects the prediction in this equation. The parameter σ denotes the width of the Euclidean distance where $\mathbf{d}_i$ can contribute to prediction.
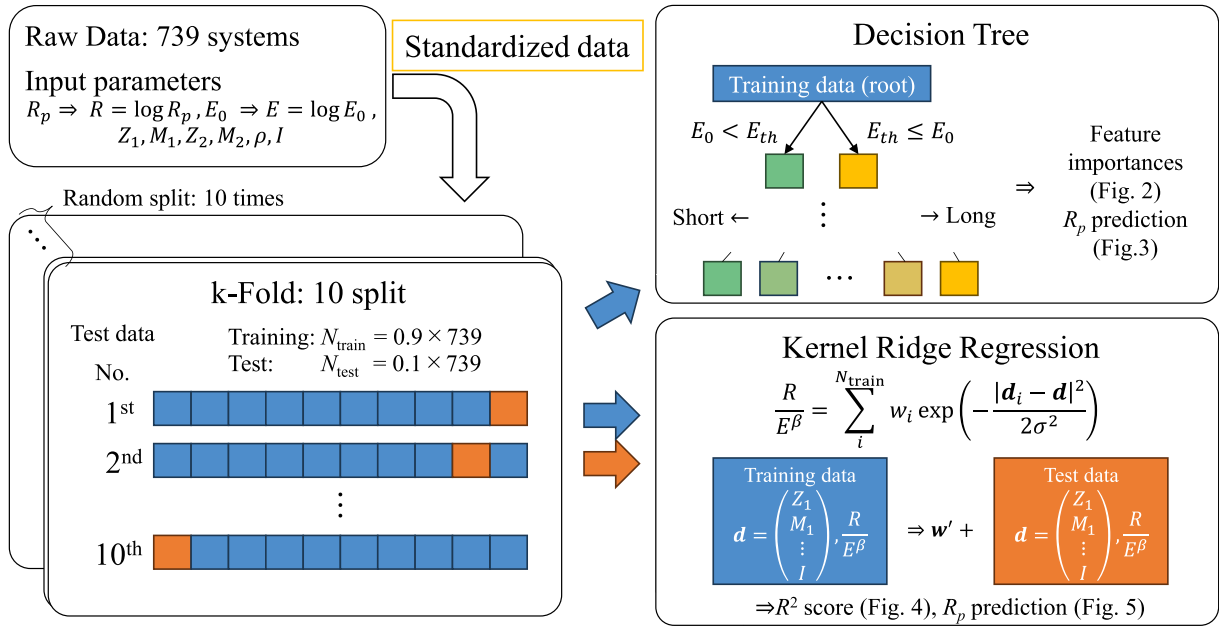
Fig. 1. Overview of data processing. Raw data were standardized before the data split. Training data and test data were chosen based on k-fold cross-validation. Decision tree and kernel ridge regression models used these training and test data.

The feature vector consists of each feature whose combination is to be examined, as shown in Fig. 1. The coefficients w_i are obtained from the learning process, which is built on minimizing the expression: $\sum_{i=1}^{N}\left(Y_i^{pred} - Y_i^{Exp}\right)^2 + \lambda\sum_{i=1}^{N}w_i^2$. Here, Y_i^{pred} is the prediction of the system in the test dataset, and Y_i^{Exp} is the corresponding objective (i.e., experimental data of the machine learning objective). The first term represents the sum of squared errors, while the second term, which includes λ, is a penalty to prevent overfitting. The explicit solution to this minimization problem is given by

third most important features were Z_1 and M_1, which are related to the implanted ion. I was the fourth most significant feature, followed by other target-related characteristics.

Fig. 3 shows the E_0 dependence of R_p for the SiC target predicted by the DTs, with the experimental values represented by symbols. Accurate prediction of R_p for the compound semiconductor is one of our challenges. Therefore, in this figure, we chose SiC as the target and B, N, Al, and P as the incident ions. These ions were chosen because they are frequently used as dopants for SiC. The filled area for each graph shows predicted R_p obtained through 10×10-time DT learnings. The filled

$$
\begin{pmatrix} w_1' \\ \vdots \\ w_i' \\ \vdots \\ w_N' \end{pmatrix} = \left[\begin{pmatrix} 1 & \cdots & K_{i1} & \cdots & K_{N1} \\ \vdots & \ddots & \vdots & \cdots & \vdots \\ K_{1i} & \cdots & 1 & \cdots & K_{Ni} \\ \vdots & \cdots & \vdots & \ddots & \vdots \\ K_{1N} & \cdots & K_{iN} & \cdots & 1 \end{pmatrix} + \lambda \begin{pmatrix} 1 & \cdots & 0 & \cdots & 0 \\ \vdots & \ddots & \vdots & \cdots & \vdots \\ 0 & \cdots & 1 & \cdots & 0 \\ \vdots & \cdots & \vdots & \ddots & \vdots \\ 0 & \cdots & 0 & \cdots & 1 \end{pmatrix} \right]^{-1} \begin{pmatrix} Y_1^{Exp} \\ \vdots \\ Y_i^{Exp} \\ \vdots \\ Y_N^{Exp} \end{pmatrix},
\tag{2}
$$

where the left-hand side vector w' is the solution (trained) vector of w, $K_{ij} = \exp\left(-|d_i - d_j|^2/2\sigma^2\right)$ with $K_{ii} = 1$, and the right-hand side vector Y^{Exp} is experimental data of the machine learning objective. The prediction uses the w' in Eq. (1), i.e., is resulted from Y^{Exp}.

3. Results

3.1. Decision tree (DT) model

As part of our research, we used the DT model to determine the significance of each feature used for prediction. We conducted k-fold cross-validation, wherein DTs were created for each k-fold dataset, and the importance of each feature was evaluated. The results are presented in Fig. 2, which shows the standard deviation of the importance obtained for each k-fold. According to the graph, the ion implantation energy E_0 was the most crucial aspect of our research. The second and

areas' upper and lower values corresponded to the predictions' maximum and minimum values. The solid line indicates their averages. This figure demonstrates that the DT model can accurately predict the R_p for experimental data. This is because all features were utilized in this model to obtain the feature importance. The predictions showed energy dependence even without available data in each graph. This indicates that the learning results for other ion-target combinations affect predictions. Therefore, the large fluctuations in the filled area observed some places can be attributed to the learning results for other ion-target combinations. It can also be observed that the energy dependence of the projected range was lost outside of a particular energy range due to the limitation of the DT model. The DT divides the R_p data into groups (branches) based on the features. The projected range was estimated based on the highest and lowest values of R_p for the energy ranges that exceed the maximum and minimum energy values in the dataset. As a result, the energy dependence was only considered within the energy
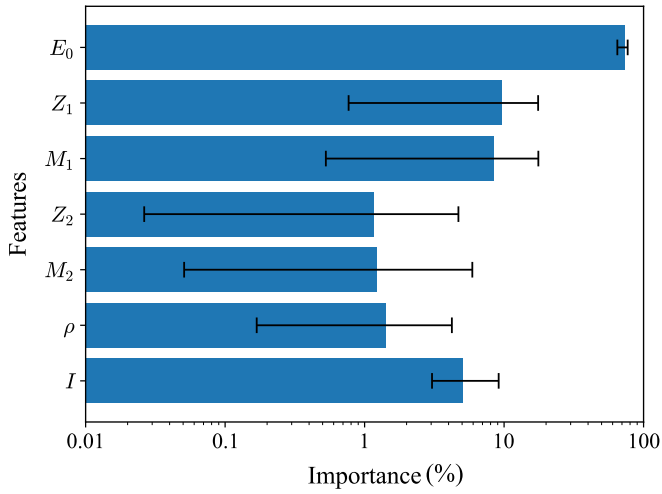
Fig. 2. Feature importance obtained from 10×10 times learning and prediction of the projected range by the DT model. E_0 is ion implantation energy, Z_1 is an atomic number of ions, M_1 is a mass number of ions, Z_2 is an atomic number of targets, M_2 is a mass number of targets, ρ is target density, and I is the mean excitation energy. Error bars show standard deviations of each importance.

range of the dataset. Therefore, the objective value needs to be adjusted from R_p.

3.2. Kernel ridge regression (KRR) model

We utilized the KRR model to establish the importance of the features associated with the targets: Z_2, M_2, ρ, and I. These features played a vital role in evaluating the DT model. The R^2 score, the coefficient of determination, was used to assess the predictive power of the feature

combination. The R^2 score is calculated as

$$R^2 = 1 - \frac{\sum_{i=1}^{N_{\text{test}}} \left(Y_i^{\text{test}} - Y_i^{\text{pred}}\right)^2}{\sum_{i=1}^{N_{\text{test}}} \left(Y_i^{\text{test}} - Y^{\text{ave}}\right)^2}$$

where Y represents the objective values for the KRR model. Here, Y_i^{pred} and Y_i^{test} are the predicted and test values, respectively, and Y^{ave} is the average of the test values.

We modified the objective value from $Y = \log R_p$ to

$$Y = \log \left(\frac{R_p}{E_0^\beta}\right), \tag{3}$$

with hyperparameter β to improve the energy dependence beyond the energy range present in the dataset. Additionally, we used other hyperparameters of σ, λ in Eq. (1), (2). The hyperparameters of σ, λ, and β were determined by making predictions using all features. We found that $\sigma = 1.95$, $\lambda = 5.2 \times 10^{-5}$, and $\beta = 1.000$.

Fig. 4 displays the R^2 score for different combinations of features related to the target material. The blue bars represent the results obtained without I, while the orange bars show the score obtained by adding I to the feature combinations. In the graph, you can see the R^2 score without target-related features. The blue bars, excluding the leftmost one representing the target-related features, show increased R^2 scores as the number of features used for learning and prediction increased. For simplicity, we'll refer to the number of features as "dimension" from here on. On the other hand, the orange bars obtained by adding I to the features showed consistently higher scores than the blue ones, indicating that I is a valid feature for accurate predictions. Interestingly, a different trend was observed in the leftmost blue and orange bars, where adding I to the feature combinations almost kept the R^2 score unchanged. Comparing each dimension, no consistent interpretations were found for the feature combinations when adding or
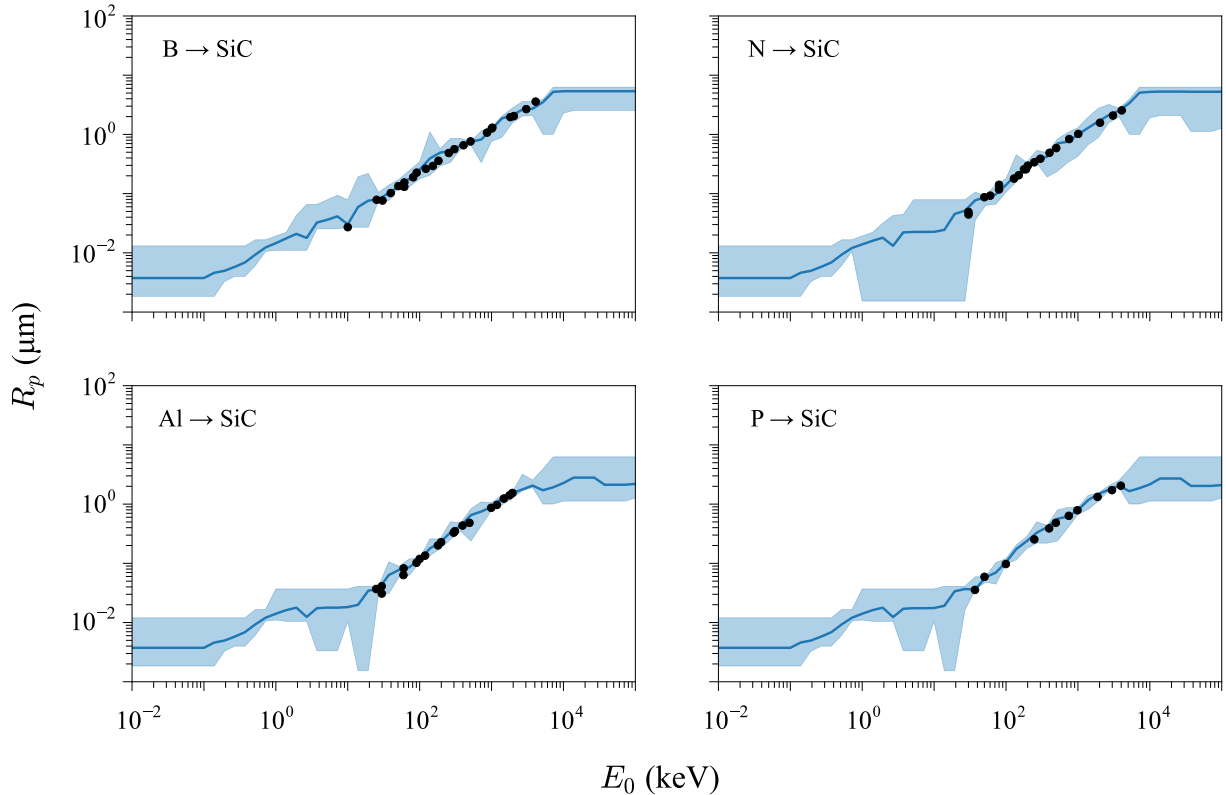
Fig. 3. DT model predictions of energy dependence of projected range of B, N, Al, P ion implantation to SiC target. Symbols are experimental data. The filled area is obtained from 10×10 times decision tree prediction. The solid line is average for them.
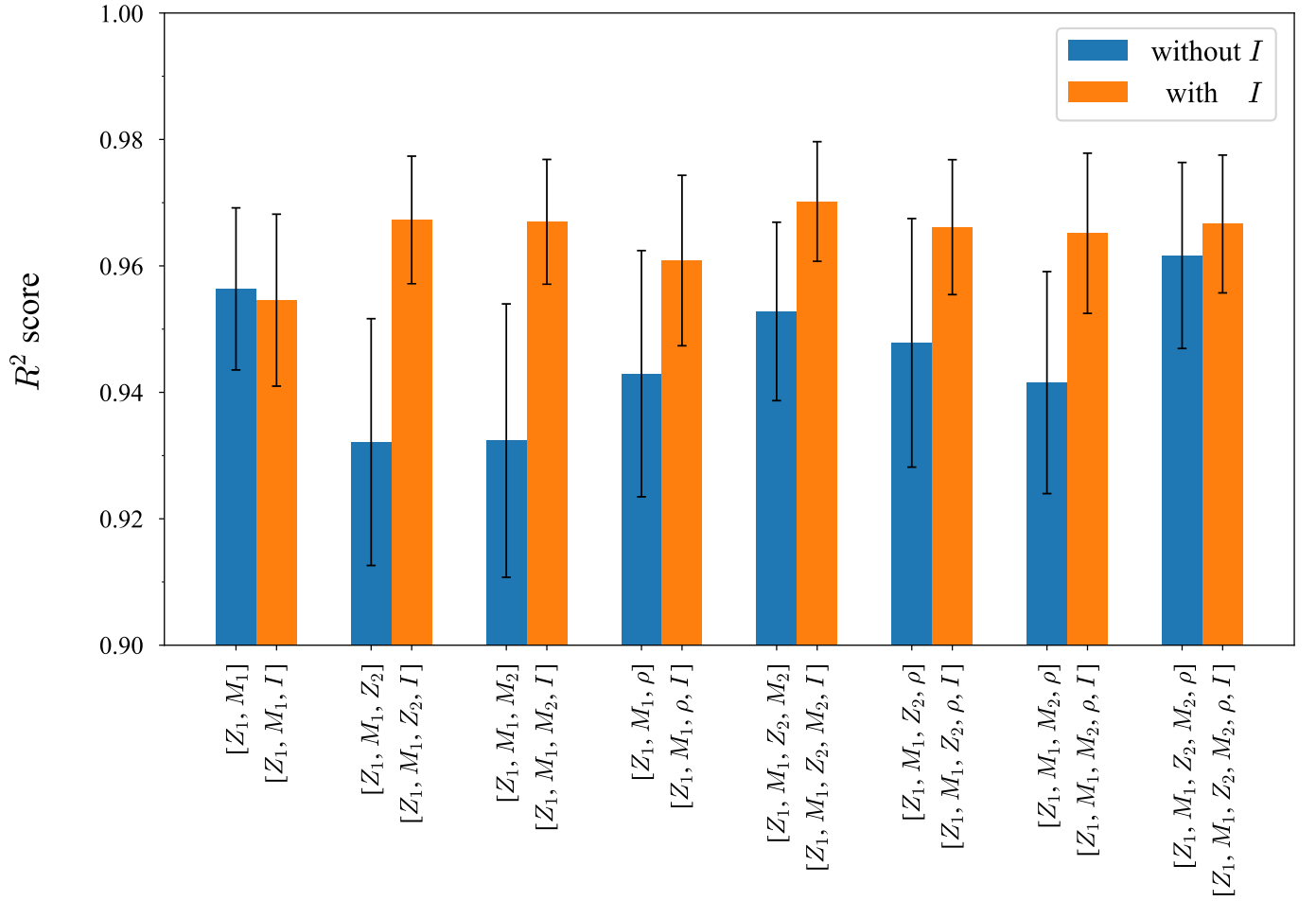
Fig. 4. R^2 scores obtained by various feature combinations using the KRR model prediction of R_p/E_0^β. Error bars show the variation of 10×10 times KRR learning. Blue bars were obtained without I. Orange bars were obtained by adding I to each feature combination. (For interpretation of the references to colour in this figure legend, the reader is referred to the web version of this article.)
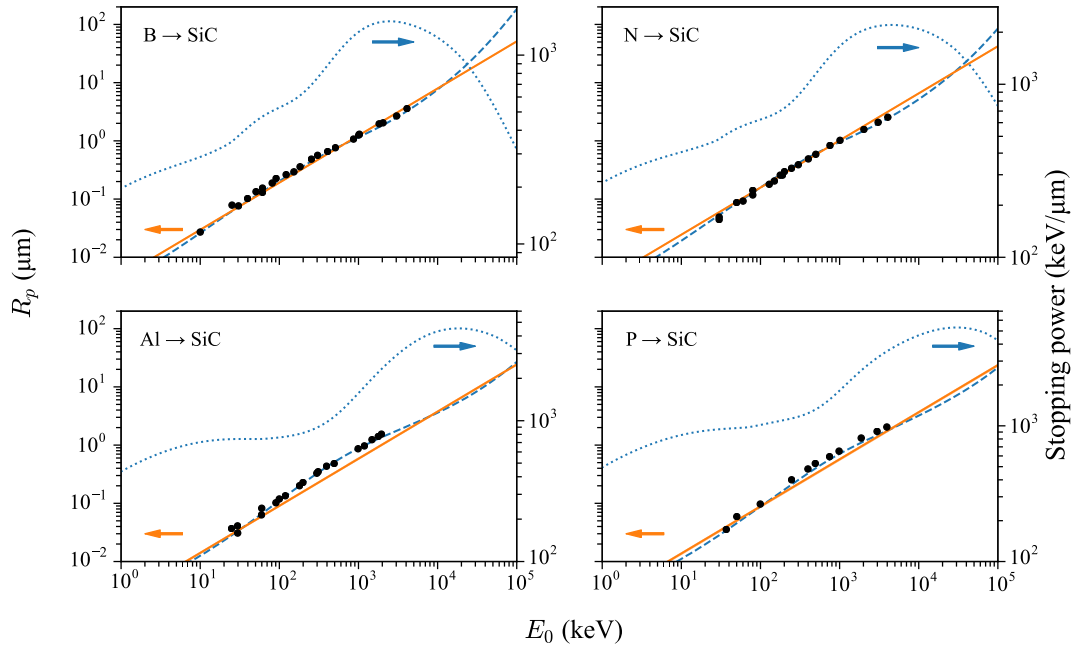
Fig. 5. R_p prediction by KRR model using features of Z_1, M_1, Z_2, M_2, ρ, and I as a function of E_0. Symbols are experimental data. Solid lines are KRR predictions for each condition. Dashed lines are SRIM predictions. Dotted lines are energy dependences of stopping power.

removing target-related features Z_2, M_2, or ρ, considering the variation in the R^2 score. Moreover, all combinations had high R^2 scores, and no combination was found to have a notably higher score than others.

Fig. 5 displays the results of KRR model predictions for the SiC target. The ion-target combinations were chosen for the same reason in Fig. 3. All features were used to make these predictions. Like the DT model predictions, the KRR model predictions were performed 10×10 times to eliminate the impact of data splitting into the training and test data. The energy dependence was obtained from the predicted results of Eq. (3). There was little variation in the KRR model predictions, possibly due to constraints on energy dependence associated with model modification. The solid lines represent the average of predicted energy dependencies. The predicted R_p consistently increased with the increase in energy, even outside the dataset, due to the model modification. The symbols show experimental values, while the dashed lines are the projected range obtained from TRIM [7]. The dotted lines depict the energy dependence of the stopping power for each ion obtained from TRIM. These dotted lines were plotted for clarity of the energy region of the stopping power. The KRR was less predictive than TRIM but agreed well with experimental data.

4. Discussion

4.1. DT model

Based on Fig. 2, the features associated with the implanted ion (Z_1 and M_1) were found to have relatively high importance. This finding aligns with the universal dependence of the reduced range on the reduced energy, as mentioned in previous studies [6]. The reduced range, denoted by r, is calculated using the formula $r = 4\pi a^2 N_d M_1 M_2 R_t / (M_1 + M_2)^2$, where a denotes Thomas-Fermi screening radius with $a = 0.8853 a_0 / \sqrt{Z_1^{2/3} + Z_2^{2/3}}$ ($a_0 = 0.5292$ Å; the Bohr radius), N_d represents the atomic number density, and R_t stands for the total range of implanted ions. On the other hand, the reduced energy, denoted by ε, is calculated using the formula $\varepsilon = M_2 a E_0 / ((M_1 + M_2) \bullet Z_1 Z_2 e^2)$ with the Thomas-Fermi screening radius a and the relation of $e^2 / 2a_0 = 13.6$[eV]. By using these reduced values, the universal dependence of r (ε) can be expressed as $r(\varepsilon) = A \varepsilon^\gamma$, where A is a constant value and γ is an ε-dependent value. According to the definition of the reduced range and energy, features related to ion and target should show the same degree of importance. However, interestingly, the features related to the target Z_2, M_2, or ρ did not show as much importance as those related to the implanted ion in this work. This could be because the variance of Z_2, M_2, or ρ in the dataset used in this study was insufficient to be as important as the features related to implanted ions.

The feature I was observed to have higher importance than other features related to the target. While the universal relation $r(\varepsilon) = A \varepsilon^\gamma$ suggested that I was unrelated to the projected range, I played a significant role in the Bethe formula of the electronic stopping power. It is important to note that Z_2 plays a significant role in the universal relationship and Bethe's electronic stopping power. As a result, the high value of I indicates that Bethe's electronic stopping power strongly impacts the projected range in the dataset used for this work.

4.2. KRR model

In Fig. 4, the validity of the I was demonstrated as the orange bars (except for the leftmost one) had higher R^2 scores than the blue ones. However, when the I was included in the feature combination of Z_1 and M_1, the R^2 score was almost unchanged (for the leftmost bars), even though they were identified as the top three essential features in the DT model. It was found that adding I and other features related to the target is necessary for accurate predictions. This finding suggests that the feature combination is crucial instead of each feature being significant. For the features Z_2, M_2, and ρ, there was no apparent difference between

the R^2 score when these features were added or removed, considering the variation of the R^2 score. A dataset with more variation in target-related features than this work might expose differences in the impact of these features on prediction accuracy.

In order to obtain the KRR model prediction shown in Fig. 5, we assumed that β is a constant value in Equation (3). We obtained $\beta = 1.000$, which indicates that the simple relationship $R_p = K E_0$ allows for somewhat accurate predictions for the dataset used in this work. However, in the energy region higher than the dataset, SRIM predictions show a steeper increase with increasing energy due to the reduction of the stopping power. This steeper increase was notably observed in B or N ion implantation to the SiC target. It is difficult to determine the difference between the steep increases observed and our prediction because TRIM relies on the semi-empirical SRIM stopping power in that energy range. However, it is important to note the change in energy dependence as the stopping power should decrease at higher energy and increase the exponential part β in E^β.

The change in the exponential part β in E^β indicates that β increases with increasing energy. Kalbitzer and Gupta previously reported this energy dependence of β. Kalbitzer showed that the exponential part for $\varepsilon < 0.02$ was $\gamma = 1/2$ and it increases to $\gamma = 2/3$ for $0.02 < \varepsilon < 0.3$ in the universal relation $r(\varepsilon) = K \varepsilon^\gamma$ [4]. Gupta also showed that γ increases with ε, and the relation is given by $\gamma = 1 + C \ln \varepsilon$, where C is the incident ion dependent value [6]. The coefficient C is reported to depend on the atomic density of the incident ion in the solid state. It is important to note that the formula $r(\varepsilon) = K \varepsilon^\gamma$ applies only to a limited range of reduced energy. Our research used a dataset that covered a wide range of energy values. Specifically, the reduced energy range in the dataset was $3.4 \times 10^{-4} < \varepsilon < 8.2 \times 10^5$. Despite the wide range of reduced energy, we could still accurately predict the R_p value. This may be because the dataset was not uniformly distributed across the entire energy range but instead concentrated in the range where the energy dependence of the R_p can be approximately proportional to the energy. Suppose we want to obtain the energy dependence in the exponential part β in E^β. In that case, we will need a more complex model and a dataset covering a uniform energy distribution across various energies for various ion and target conditions.

5. Conclusion

We studied predicting the range of implanted ions using two machine-learning models. The decision tree model was used to determine the importance of each feature, while the kernel ridge regression model evaluated combinations of features. We found that simple features can provide accurate predictions, including Z_1, M_1, Z_2, M_2, ρ, and I. However, it was also found that combinations of features are crucial in obtaining accurate predictions. We also found that including the mean excitation energy improved the accuracy of projected range predictions, but adding only this feature did not lead to any improvements. Finally, we noted that the relationship $R_p = K E_0$ was limited to the lower energy region of the dataset, and further modifications to the objective for machine learning are required to obtain validity in wider energy regions.

Appendix 1

Table A1
Reference list of incident ion range data using in this study.

Target	Ion	Ref.
C	H	[18]
	Li	[19]
	B	[19,20]
	N	[21,22]
	O	[23]
	Ne	[21,23]
	Mg	[24]
	Al	[24,25]
	P	[24]
	S	[24]
	Cl	[24]
	K	[24]
	Ar	[21,24–27]
	Cr	[24]
	Mn	[24]
	Cu	[24]
	Zn	[24]
	Ga	[24]
	As	[24]
	Br	[24]
	Kr	[24,25,27]
	Rb	[24]
	Ag	[24]
	In	[24]
	Sn	[24]
	Sb	[24,28]
	I	[24]
	Te	[24]
	Xe	[24,25,27]
	Cs	[24]
	Ba	[24]
	Eu	[29]
	Er	[29]
	Yb	[29]
	Au	[24,26]
	Hg	[24]
	Tl	[24]
	Pb	[24,29]
	Bi	[24,25,30]
	U	[31]
Si	H	[32]
	B	[33]
	N	[32,33]
	Al	[34]
	P	[33,34]
	Ga	[34]
	As	[34]
	Sb	[34]
	Bi	[34]
V	He	[35,36]
	Li	[37]
	N	[22,38]
	Xe	[27]
Ge	H	[32]
	B	[32]
	Si	[32]
Zr	He	[36]
	N	[22,39]
Ag	H	[40]
	He	[41]
	Si	[42]
	Ni	[42]
	Au	[42]
W	He	[43,44]
	K	[45]
Au	He	[41]
	C	[46]
	F	[46]
	Cl	[46]
	Ti	[46]
	Fe	[46]

Table A1 (*continued*)

Target	Ion	Ref.
	Cu	[46]
	Zn	[46]
	Cu	[46]
	Mo	[46]
	Ag	[46]
	Ce	[47]
	Au	[46]
U	H	[48]
LiF	H	[49]
	He	[49]
MgO	He	[36]
Al_2O_3	H	[50]
	O	[51]
	Zn	[52]
	Ga	[52]
	As	[52]
	Se	[52]
	Cd	[52]
	Te	[52]
	Xe	[5]
	Au	[5]
	Pb	[5]
	Bi	[5]
SiC	H	[10,53]
	Li	[10]
	B	[10,54–56]
	N	[10,54–59]
	O	[10]
	Al	[10,54,55,57–59]
	P	[10,57–59]
	Ga	[10,60]
	As	[10,54]
	Au	[8]
Si_3N_4	Zn	[52]
	Ga	[52]
	Se	[52]
	Cd	[52]
	Te	[52]
SiO_2	H	[61]
	He	[61,62]
	B	[63–67]
	O	[61]
	Ne	[61]
	Ar	[61]
	Zn	[52]
	Ga	[52]
	As	[29,52,65,68,69]
	Se	[52]
	Cd	[52]
	Te	[52]
	Xe	[29]
	Cs	[29,70]
	Eu	[29]
	Yb	[29]
	Au	[30]
	Bi	[30]
GaN	H	[71]
	Li	[71]
	Be	[71]
	C	[71]
	F	[71]
	Na	[71]
	Mg	[71]
	Si	[71]
	S	[71]
	Zn	[71]
	Ge	[71]
	Se	[71]
GaP	N	[72]
	P	[72]
GaAs	H	[73]
	He	[73]
	C	[74]
	N	[72]
	F	[75]
	Ne	[76]

Table A1 (*continued*)

Target	Ion	Ref.
	Mg	[77]
	Si	[78,79]
	P	[72]
	S	[17,80]
	Ar	[76]
	Kr	[76]
InSb	He	[41]

References

[1] M. Nastasi, J. Mayer, J.K. Hirvonen, *Ion-Solid Interactions: Fundamentals and Applications*, Cambridge University Press, Cambridge, 1996. https://doi.org/10.1017/CBO9780511565007.

[2] J.F. Ziegler, *Handbook of ION IMPLANTATION TECHNOLOGY*. North-Holland, Elsevier Science Publishers B. V., 1992. 700 S. 307 Abb. 28 Tab. ISBN 0-444-89735-6, Cryst. Res. Technol. 28 (1993) 978–978. https://doi.org/10.1002/crat.2170280719.

[3] B.L. Crowder, ed., *Ion Implantation in Semiconductors and Other Materials*, Springer US, Boston, MA, 1973. https://doi.org/10.1007/978-1-4684-2064-7.

[4] S. Kalbitzer, H. Oetzmann, Ranges and range theories, Radiat. Eff. 47 (1980) 57–71, https://doi.org/10.1080/00337578008209189.

[5] K. Izsak, J. Berthold, S. Kalbitzer, Nucl. Instrum. Methods Phys. Res. Sect. B 15 (1986) 34–41, https://doi.org/10.1016/0168-583X(86)90247-8.

[6] S.K. Gupta, P.K. Bhattacharya, Phys. Rev. B 29 (1984) 2449–2457, https://doi.org/10.1103/PhysRevB.29.2449.

[7] J. Zieglar, J.F. Biersack, U. Littmark, The Transport of Ions in Matter (TRIM) Monte-Carlo Calculation Including in Computer Program SRIM Version, 2010, www.SRIM.org.

[8] K. Jin, Y. Zhang, Z. Zhu, D.A. Grove, H. Xue, J. Xue, W.J. Weber, J. Appl. Phys. 115 (2014) 044903, https://doi.org/10.1063/1.4861642.

[9] K. Jin, Y. Zhang, H. Xue, Z. Zhu, W.J. Weber, Nucl. Instrum. Methods Phys. Res. Sect. B 307 (2013) 65–70, https://doi.org/10.1016/j.nimb.2013.02.051.

[10] M.S. Janson, M.K. Linnarsson, A. Hallén, B.G. Svensson, J. Appl. Phys. 93 (2003) 8903–8909, https://doi.org/10.1063/1.1569666.

[11] W.A. Parfitt, R.B. Jackman, Nucl. Instrum. Methods Phys. Res. Sect. B 478 (2020) 65–70, https://doi.org/10.1016/j.nimb.2020.05.015.

[12] F.B. Haiek, A.M.P. Mendes, C.C. Montanari, D.M. Mitnik, J. Appl. Phys. 132 (2022) 245103, https://doi.org/10.1063/5.0130875.

[13] X-Ray Mass Attenuation Coefficients, NIST (2009). https://dx.doi.org/10.18434/T4D01F (accessed December 31, 2023).

[14] L. Breiman, J.H. Friedman, R.A. Olshen, C.J. Stone, *Classification and Regression Trees*, Chapman and Hall/CRC., Routledge, New York, 1984. https://doi.org/10.1201/9781315139470.

[15] F. Pedregosa, G. Varoquaux, A. Gramfort, V. Michel, B. Thirion, O. Grisel, M. Blondel, P. Prettenhofer, R. Weiss, V. Dubourg, J. Vanderplas, A. Passos, D. Cournapeau, Scikit-learn: Machine Learning in Python, J. Mach. Learn. Res. 12 (2011) 2825–2830.

[16] K.P. Murphy, Machine learning: a probabilistic perspective, MIT Press, Cambridge, MA, 2012.

[17] R.G. Wilson, D.M. Jamba, V.R. Deline, C.A. Evans Jr., Y.S. Park, J. Appl. Phys. 54 (1983) 3849–3854, https://doi.org/10.1063/1.332609.

[18] R. Mather, E. Segrè, Phys. Rev. 84 (1951) 191–193, https://doi.org/10.1103/PhysRev.84.191.

[19] D. Fink, J.P. Biersack, J.T. Chen, M. Städele, K. Tjan, M. Behar, C.A. Olivieri, F. C. Zawislak, J. Appl. Phys. 58 (1985) 668–676, https://doi.org/10.1063/1.336180.

[20] B. Blanchard, J.L. Combasson, J.C. Bourgoin, Appl. Phys. Lett. 28 (1976) 7–8, https://doi.org/10.1063/1.88573.

[21] D. Powers, W. Whaling, Range of Heavy Ions in Solids, Phys. Rev. 126 (1962) 61–69, https://doi.org/10.1103/PhysRev.126.61.

[22] D.J. Land, D.G. Simons, J.G. Brennan, M.D. Brown, Phys. Rev. A 22 (1980) 68–75, https://doi.org/10.1103/PhysRevA.22.68.

[23] W.K. Chu, P.D. Bourland, K.H. Wang, D. Powers, Phys. Rev. 175 (1968) 342–353, https://doi.org/10.1103/PhysRev.175.342.

[24] D.C. Santry, R.D. Werner, O.M. Westcott, IEEE Trans. Nucl. Sci. 26 (1979) 1331–1334, https://doi.org/10.1109/TNS.1979.4330381.

[25] D.C. Santry, R.D. Werner, Nucl. Instrum. Methods 139 (1976) 135–146, https://doi.org/10.1016/0029-554X(76)90668-6.

[26] F. Abel, M. Behar, C. Cohen, Nucl. Instrum. Methods Phys. Res. Sect. B 30 (1988) 13–15.

[27] D. Powers, W.K. Chu, P.D. Bourland, Phys. Rev. 165 (1968) 376–387, https://doi.org/10.1103/PhysRev.165.376.

[28] G. Braunstein, T. Bernstein, U. Carsenty, R. Kalish, J. Appl. Phys. 50 (1979) 5731–5735, https://doi.org/10.1063/1.326710.

[29] P.L. Grande, P.F.P. Fichtner, M. Behar, F.C. Zawislak, Nucl. Instrum. Methods Phys. Res. B 35 (1988) 17–20.

[30] P.L. Grande, P.F.P. Fichtner, M. Behar, R.P. Livi, F.C. Zawislak, J.P. Biersack, D. Fink, P. Mertens, Nucl. Instrum. Methods Phys. Res. B 19 (20) (1987) 25–27.

[31] Y. Laichter, H. Geissel, M. Schädel, P. Armbruster, Phys. Rev. A 26 (1982) 1915–1923, https://doi.org/10.1103/PhysRevA.26.1915.

[32] V. Schüle, R. Günzler, P. Oberschachtsiek, M. Weiser, S. Kalbitzer, Nucl. Instrum. Methods Phys. Res. Sect. B 62 (1992) 338–345, https://doi.org/10.1016/0168-583X(92)95253-N.

[33] S. Roosild, R. Dolan, B. Buchanan, J. Electrochem. Soc. 115 (1968) 307, https://doi.org/10.1149/1.2411148.

[34] B.L. Crowder, J. Electrochem. Soc. 118 (1971) 943–952, https://doi.org/10.1149/1.2408229.

[35] R.S. Blewer, J. Nucl. Mater. 53 (1974) 268–275, https://doi.org/10.1016/0022-3115(74)90255-4.

[36] M.B. Lewis, W.R. Allen, Nucl. Instrum. Methods Phys. Res. B 35 (1988) 10–16.

[37] B. Emmoth, M. Braun, H.P. Palenius, J. Nucl. Mater. 63 (1976) 482–486.

[38] D.G. Simons, D.J. Land, J.G. Brennan, M.D. Brown, Phys. Rev. A 12 (1975) 2383–2392, https://doi.org/10.1103/PhysRevA.12.2383.

[39] D. Fink, J.P. Biersack, M. Städele, K. Tjan, V.K. Cheng, Nucl. Instrum. Methods Phys. Res. 218 (1983) 171–175, https://doi.org/10.1016/0167-5087(83)90975-4.

[40] H. Bichsel, R.F. Mozley, W.A. Aron, Phys. Rev. 105 (1957) 1788–1795, https://doi.org/10.1103/PhysRev.105.1788.

[41] G.W. Gobeli, Phys. Rev. 103 (1956) 275–278, https://doi.org/10.1103/PhysRev.103.275.

[42] J.M. Anthony, W.A. Lanford, Nucl. Instrum. Methods 186 (1981) 647–654.

[43] D.N. Seidman, The study of defects and radiation damage in solids by field-ion and atom-probe microscopy, Cornell University, Master, 1979.

[44] A. Wagner, D.N. Seidman, Phys. Rev. Lett. 42 (1979) 515–518, https://doi.org/10.1103/PhysRevLett.42.515.

[45] L. Eriksson, Phys. Rev. 161 (1967) 235–244, https://doi.org/10.1103/PhysRev.161.235.

[46] R.A. Schmitt, R.A. Sharp, Phys. Rev. Lett. 1 (1958) 445–447, https://doi.org/10.1103/PhysRevLett.1.445.

[47] K. Güttner, S. Hofmann, D. Marx, G. Münzenberg, F. Nickel, Nucl. Instrum. Methods 146 (1977) 413–417, https://doi.org/10.1016/0029-554X(77)90727-3.

[48] M.B. Lewis, J. Nucl. Mater. 88 (1980) 23–30.

[49] K. Kubo, J. Phys. Soc. Jpn. 36 (1974) 1593–1596.

[50] J. Bøttiger, J.R. Leslie, N. Rud, J. Appl. Phys. 47 (1976) 1672–1675, https://doi.org/10.1063/1.322791.

[51] P.D. Croft, K. Street Jr., Phys. Rev. 165 (1968) 1375–1380, https://doi.org/10.1103/PhysRev.165.1375.

[52] W.K. Chu, B.L. Crowder, J.W. Mayer, J.F. Ziegler, Appl. Phys. Lett. 22 (1973) 490–492, https://doi.org/10.1063/1.1654480.

[53] L. Leblanc, L.G. Ross, Nucl. Instrum. Methods Phys. Res. Sect. B 114 (1996) 203–207, https://doi.org/10.1016/0168-583X(95)01573-6.

[54] S. Ahmed, C.J. Barbero, T.W. Sigmon, J.W. Erickson, J. Appl. Phys. 77 (1995) 6194–6200, https://doi.org/10.1063/1.359146.

[55] R. Stief, M. Lucassen, R. Schork, H. Ryssel, K.-H. Hölzlein, R. Rupp, D. Stephani, IEEE, New York, 1999: p. 760.

[56] R. Lossy, W. Reichert, E. Mater, Sci. Eng. B 46 (1997) 156–159, https://doi.org/10.1016/S0921-5107(96)01968-X.

[57] M.V. Rao, P. Griffiths, O.W. Holland, G. Kelner, J.A. Freitas Jr., D.S. Simons, P. H. Chi, M. Ghezzo, J. Appl. Phys. 77 (1995) 2479–2485, https://doi.org/10.1063/1.358776.

[58] M.V. Rao, J.A. Gardner, P.H. Chi, O.W. Holland, G. Kelner, J. Kretchmer, M. Ghezzo, J. Appl. Phys. 81 (1997) 6635–6641, https://doi.org/10.1063/1.365236.

[59] J. Gaedner, M.V. Rao, O.W. Holland, G. Kelner, D.S. Simons, P.H. Chi, J. M. Andrews, J. Kretchmer, M. Ghezzo, J. Electron. Mater. 25 (1996) 885–892, https://doi.org/10.1007/BF02666654.

[60] M. Behar, P.F.P. Fichtner, P.L. Grande, F.C. Zawislak, Mater. Sci. Eng. R Rep. 15 (1995) 1–83, https://doi.org/10.1016/0927-796X(94)00176-6.

[61] E.P. EerNisse, J. Appl. Phys. 45 (1974) 167–174, https://doi.org/10.1063/1.1662952.

[62] R.L. Hines, Phys. Rev. 120 (1960) 1626–1630, https://doi.org/10.1103/PhysRev.120.1626.

[63] L.-O. Bauer, M.R. Macpherson, A.T. Robinson, H.G. Dill, Solid-State Electron. 16 (1973) 289–300.

[64] M.Y. Darwish, H.W. Luginbühl, Appl. Phys. Lett. 25 (1974) 390–391, https://doi.org/10.1063/1.1655520.

[65] R. Schimko, C.E. Richter, K. Rogge, G. Schwarz, M. Trapp, Phys. Status Solidi A 28 (1975) 87–93, https://doi.org/10.1002/pssa.2210280108.

[66] N.G. Blamires, B.J. Smith, J. Phys. Appl. Phys. 10 (1977) 799–804.

[67] V. Rybka, V. Hnatowicz, J. Kvítek, J. Vacík, B. Schmidt, Determination of the range profiles of boron implanted into Si and SiO2, Phys. Status Solidi A 83 (1984) 165–171, https://doi.org/10.1002/pssa.2210830118.

[68] K. Tsukamoto, Y. Akasaka, K. Horie, Jpn. J. Appl. Phys. 16 (1977) 663–664, https://doi.org/10.1143/JJAP.16.663.

[69] J. Nakata, K. Kajiyama, Jpn. J. Appl. Phys. 21 (1982) 1363–1369, https://doi.org/10.1143/JJAP.21.1363.

[70] B.J. Fishbein, J.D. Plummer, J. Appl. Phys. 63 (1988) 5887–5889, https://doi.org/10.1063/1.340283.

[71] R.G. Wilson, C.B. Vartuli, C.R. Abernathy, S.J. Pearton, J.M. Zavada, Solid-State Electron. 38 (1995) 1329–1333, https://doi.org/10.1016/0038-1101(94)00251-A.

[72] A.H. Kachare, W.G. Spitzer, J.E. Fredrickson, F.K. Euler, J. Appl. Phys. 47 (1976) 5374–5381, https://doi.org/10.1063/1.322564.

[73] J. Räisänen, E. Rauhala, Nucl. Instrum. Methods Phys. Res. B 93 (1994) 1–4.

[74] B.K. Shin, J.E. Ehret, Y.S. Park, M. Stefiniw, J. Appl. Phys. 49 (1978) 2988–2990, https://doi.org/10.1063/1.325146.

[75] J.S. Harris, J.M. Harris, H.L. Marcus, Appl. Phys. Lett. 21 (1972) 598–601, https://doi.org/10.1063/1.1654270.

[76] W.J. Anderson, Y.S. Park, J. Appl. Phys. 49 (1978) 4568–4570, https://doi.org/10.1063/1.325471.

[77] Y.K. Yeo, Y.S. Park, P.W. Yu, J. Appl. Phys. 50 (1979) 3274–3281, https://doi.org/10.1063/1.326367.

[78] D.H. Lee, R.M. Malbon, Appl. Phys. Lett. 30 (1977) 327–329, https://doi.org/10.1063/1.89386.

[79] J. Kasahara, M. Arai, N. Watanabe, J. Appl. Phys. 50 (1979) 8229–8231, https://doi.org/10.1063/1.325922.

[80] Y.S. Park, J.T. Grant, T.W. Haas, J. Appl. Phys. 50 (1979) 809–812, https://doi.org/10.1063/1.326048.